6

Thin-Film III–V Single Junction and Multijunction Solar Cells and Their Integration onto Heterogeneous Substrates

He Ding[1] and Xing Sheng[2]

[1] *Beijing Institute of Technology, School of Optics and Photonics, 5 South Zhongguancun Street, Beijing, 100081, China*
[2] *Tsinghua University, Department of Electronic Engineering and Beijing National Research Center for Information Science and Technology, 30 Shuangqing Street, Beijing, 100084, China*

6.1 Introduction

Over the last decade, thanks to technology developments and economies of scale, the photovoltaic (PV) industry has been booming with growth rates well in excess of 30% per year and the PV system cost is continuously reduced by approximately 20% each time the cumulative production doubled [1–3]. In spite of the high growth rate and the lower price, the PV industry is still dependent on subsidies in the major markets of the world, which is highly affected by government policies [3]. In order to further develop the PV market and attract more industrial companies, costs should be further reduced and solar cell efficiencies should be enhanced, in order to overcome grid parity [4]. Among all the PV techniques, III–V-based solar cells are the most successful technique for achieving the highest PV conversion efficiencies, mainly attributed to their unique characteristics such as high crystallinity and strong optical absorption. In particular, multijunction (MJ) III–V-based solar cells make the best use of the broadband solar spectrum by utilizing multiple optically and electrically coupled subcells with different bandgaps, and their performance is steadily improved by absolute ~1% efficiency increase per year, with the recent record efficiency reaching 46% [1] (https://www.nrel.gov/pv/).

   III–V solar cell structures are conventionally grown on thick single crystalline semiconductor substrates, which significantly inhibit the mechanical flexibility of the solar cells and limit their specific power per weight [5]. Recently developed thin-film III–V solar cells based on flexible substrates represent an attractive class of PV devices in terms of their high performance, light weight, and the ease of heterogeneous integration with other systems such as wearable, portable, and deployable devices [6–8]. Nowadays, thin-film, high-efficiency III–V solar cells on flexible substrates have attracted enormous interest in applications such as terrestrial and space solar energy harvest, power supplies for unmanned aerial vehicles (UAVs), and healthcare systems [9–12].

6.2 III–V Solar cells

6.2.1 Single Junction Solar Cells

According to the Shockley–Queisser (SQ) theory [13], the limiting PV energy conversion efficiency for a single junction solar cell is 33.7% with an optimum semiconductor bandgap of 1.34 eV. Figure 6.1 shows the maximum theoretical efficiency of the single p–n junction solar cell with different bandgap materials and some of the record efficiencies under the standard AM1.5g solar spectrum illumination [1, 13]. In order to approach the thermodynamic efficiency limits, solar cells should employ perfect semiconducting materials, as well as ideal electronic and optical structures to capture as many photons as possible and effectively convert them into free carriers that can generate electricity [14].

6.2.1.1 GaAs

Gallium arsenide (GaAs) is a typical III–V direct-bandgap semiconductor material, which has a bandgap of about 1.42 eV. Among all types of single junction solar cells, GaAs solar cells experimentally demonstrate the highest power conversion efficiency and approach the SQ limit (Figure 6.1) [1]. The efficiency record of GaAs solar cells has been constantly broken over the past several years. Most GaAs solar cells with high conversion efficiency that have been reported so far use semiconductor materials with exceptionally high quality for relatively thick absorbers with smooth top surfaces and rear mirrors. Steiner et al. have fabricated high-quality GaAs solar cells with back reflectance, achieving high conversion efficiencies around 27.8 % and an increased open-circuit voltage of 1.1 V under the global solar spectrum [15]. In such cells, strong photon recycling effects with high back reflectance increase the equilibrium density of minority carriers, with a corresponding increase in the radiative lifetime. Thus, it dramatically increases the external luminescence-yielding cells, resulting in high efficiency.

In order to further increase the efficiency and reduce manufacturing cost, thin-film GaAs solar cells have been focused and studied. Using commonly available materials with routinely achievable quality, it becomes necessary
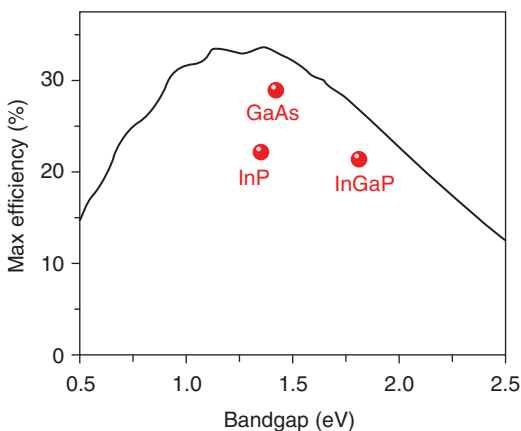

Figure 6.1 Theoretical Shockley–Queisser (SQ) detailed balance efficiency limit as a function of bandgap for single junction solar cells under AM1.5g illumination [13]. The points represent the record efficiencies for the typical III–V cells including GaAs, InP, and InGaP [1, 14].

to implement light management structures (e.g. textured surface) to achieve maximum absorption and minimum nonradiative recombination in a thin absorber. Recently, Alta Devices Inc. has achieved a new certified world record efficiency of 28.8% for single junction GaAs solar cells under AM1.5g illumination [1, 16]. The improved efficiency is mainly due to enhanced photon recycling in the thin-film cell architecture by using pristine semiconductors and highly reflective mirrors, which in turn result in high open-circuit voltages. By taking advantage of the epitaxial lift-off (ELO) process [17], the thin-film device on a flexible substrate was made from its grown single-crystal GaAs handle substrates, which can be subsequently reused for another growth for significant cost reduction.

6.2.1.2 InP

Crystalline indium phosphide (InP) is another important III–V compound semiconductor for PV devices, whose bandgap of 1.35 eV lies close to the optimum for single junction solar cells. Even though the current efficiency of InP solar cells is less than that demonstrated for GaAs ones due to their lower open-circuit voltages and fill factors, they still offer a suitable option for both space and terrestrial PV applications, especially for the MJ solar system. In addition, the inherently high resistance of InP to radiation damage gives it a special advantage for space applications compared to GaAs or silicon materials [18].

There has been significant interest in the development of InP solar cell technology for several years after the discovery of its high radiation resistance during the middle 1980s [19]. Several years later, Keavney et al. have shown the most efficient InP solar cells using a homojunction configuration fabricated by metal–organic vapor deposition (MOCVD), reaching efficiencies of up to 22.1% [20]. Nowadays, an efficiency of 24.2% has been reported for a 1 cm^2 InP cell fabricated and measured at the US National Renewable Energy Laboratory (NREL) [21]. Furthermore, the composing of InP with other materials, e.g. TiO$_2$, to form the heterojunction solar cell has been reported by Yin et al. in 2014 [22]. With improved long-wavelength response through hydrogen plasma treatment of the InP surface, the InP heterojunction solar cell with electron-selective TiO$_2$ contact has a high short-circuit current density of 30.5 mA/cm^2 and a high power conversion efficiency of 19.2%.

6.2.1.3 InGaP

Indium gallium phosphide (InGaP) is a semiconductor composed of indium, gallium, and phosphorus, which is almost lattice matched to GaAs [23]. The bandgap of InGaP is influenced by the growth conditions, and values ranging from 1.80 eV for an ordered lattice to 1.9–2.0 eV for a disordered one have been reported [24–26]. Geisz et al. demonstrated a bandgap of 1.81 eV for InGaP single junction solar cells approaching the SQ limit with 20.8% solar conversion efficiency at AM1.5g conditions, which is mainly attributed to a higher bandgap AlInGaP layer and the back metal reflector [27]. This rear heterojunction design can also result in significant voltage improvement in inverted MJ solar cells.

Single junction InGaP solar cells could not benefit from all the light photons, and the maximum wastage is of the photons of energy much above and below the

bandgap. Several strategies including multijunction or enhanced single junction solar cells have been proposed to fully profit from the solar spectrum to have higher conversion efficiency. Yang et al. recently reported that an optical design with a reflective backscattering layer can potentially offer the maximal conversion efficiency for double-heterostructure (DH) single junction solar cells. The final $In_{0.49}Ga_{0.51}P/GaAs/In_{0.49}Ga_{0.51}P$ solar cells were monolithically integrated with a lattice-matched $Al_{0.52}In_{0.48}P$ substrate coated with a Au reflector, achieving an efficiency of 19.1% under AM1.5g illumination [28]. Sheng et al. introduced a Eu-based phosphor doped poly(methyl methacrylate) (PMMA) on the surface of the single junction InGaP cells, increasing the cells' spectral responses at wavelengths between 300 and 360 nm by downshifting ultraviolet (UV) light into the visible range [7].

As introduced previously, a thin-film GaAs solar cell holds record single junction efficiency at 28.8% under 1-sun AM1.5d illumination [16] and InGaP solar cells have been tailored to reach efficiency values exceeding 20% [27]. With satisfactory quality and performance, as well as appropriate bandgap energy, InGaP has been regarded as the most promising top layer in the MJ structure to absorb high-energy photons and will be introduced in the following sections.

6.2.2 Double Junction Cells

6.2.2.1 InGaP/GaAs

As shown in Figure 6.2a, single junction solar cells can only have a maximum work condition when absorbing a certain wavelength of photons, the energy of which is equal to the bandgap ($h\nu = E_g$). For incident light with a photon energy higher than the cell bandgap ($h\nu > E_g$), only part of the photon energy can be converted to electrical energy and the remaining excess energy ($h\nu - E_g$) is wasted as thermalization loss. On the other hand, photons with energies lower than the bandgap ($h\nu < E_g$) cannot be absorbed and converted into electricity. Since PV cells are operated under broadband solar irradiation with photons at wavelengths from ultraviolet to infrared (300–1700 nm), such thermalization loss and sub-bandgap transparency result in low efficiencies in single junction solar cells. To overcome this obstacle of energy loss in solar cells, MJ PV structures that comprise subcells with different bandgaps are developed.

Figure 6.2b schematically presents the operation principal of a typical MJ solar cell, in which the broadband sunlight penetrates into multiple cells, with high-energy photons being absorbed by the top cells with large bandgaps and low-energy photons absorbed by the corresponding lower cells with small bandgaps. Conventional MJ solar cells are formed by epitaxial growth methods, with each subcell being electrically connected in series. To obtain MJ solar cells with ideal efficiencies, issues including lattice matching and current matching among the subcell junctions are to be considered.

Double junction (2J) AlGaAs/GaAs solar cells were first developed in early days, and efficiencies less than 20.2% were achieved due to low performance and unstable tunnel junctions, and the defects related to the oxygen in the AlGaAs materials [30]. Thus, a tandem combination of InGaP material for the top cell with GaAs cell in the bottom was proposed by Olson et al. [31]. With
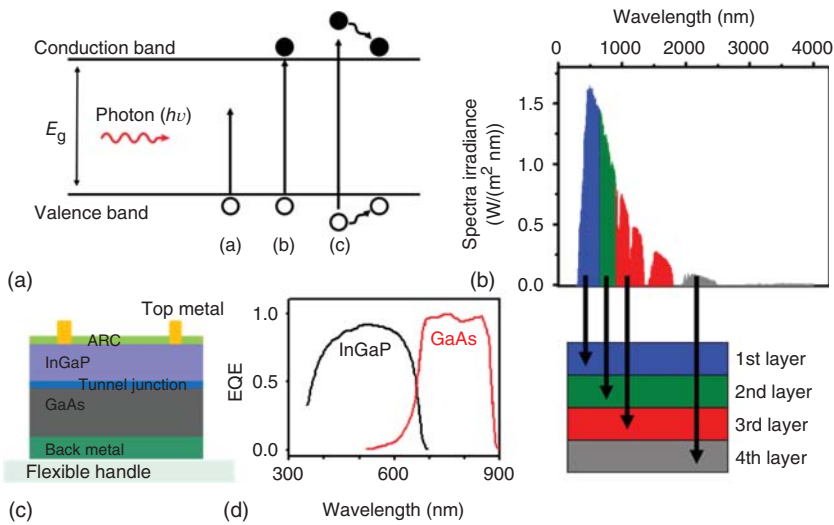
Figure 6.2 (a) Schematic illustration of the electron–hole pairs generation process in the bandgap material (E_g) excited by light photons with different energies ($h\upsilon$). (b) Schematic illustration of the absorption of solar spectrum for each subcell in multijunction (MJ) solar cells. (c) Schematic illustration of flexible InGaP/GaAs tandem solar cells, (d) and the corresponding EQE spectrum of each subcell. Source: Reproduced with permission [8, 29]. Copyright 1997, AIP Publishing LLC.

the improved performance on the tunnel junction between the subcells and top cell of the InGaP layer in the epitaxial growth process, Takamoto et al. achieved InGaP/GaAs tandem cells with an efficiency over 30% under AM1.5g illumination [29, 32]. In 2013, Alta Device Inc. reported a 30.8% efficiency 2J InGaP/GaAs solar cell as shown in Figure 6.2c [8]. In the same year, NREL achieved a new record of 31.1% under AM1.5g illumination with improved voltage in the bottom cell, mainly due to the enhanced photon recycling effect with a gold back mirror contact [33]. By far, NREL demonstrated a world record 32.6% efficiency of 2J solar cells under AM1.5g illumination, which is made of the 1.7 eV InGaAsP top cell and 1.1 eV InGaAs bottom cell as well as a transparent buffer layer of AlInGaAs in between by atmospheric pressure metal–organic vapor-phase epitaxy (MOVPE) method [34]. Owing to the excellent materials qualities and close-to-optimal bandgap of 1.6/0.9 eV, higher efficiency could be obtained compared to the InGaP/GaAs (∼1.9/1.42 eV) 2J case.

The external quantum efficiency (EQE) spectra of each subcell in a typical InGaP/GaAs cell are shown in Figure 6.2d, indicating the fraction of the incident light of given wavelengths that are converted into electricity [8]. Furthermore, the InGaP/GaAs cells have great potential for future space applications and have shown superior radiation-resistant properties in comparison to single junction solar cells [35].

The 2J solar cells serve as a starter for MJ cell research, and then triple, quadruple, and even more than four junction (4J)-based cells have been designed to further make the best use of the entire solar spectrum. With the development

of material properties and advanced concept designs, efficiency record-breaking has been occurring continuously recently, with an absolute efficiency increase of about 1% each year [5].

6.2.3 Triple Junction Cells

6.2.3.1 InGaP/GaAs/Ge

As stated previously, the InGaP/GaAs 2J solar cells have a theoretical efficiency of 36.4% under 1000-sun AM1.5d illumination [36], because part of the solar spectrum, especially for wavelengths longer than 900 nm, still cannot be fully absorbed. Thus, a third subcell with a lower bandgap is needed on the rear side of the 2J solar cells, forming a triple junction (3J) cell structure. Currently, the most widely used high-efficiency III–V solar cells utilize a three junction design that includes a germanium (Ge) cell in conjunction with lattice-matched InGaP and GaAs top junction cells. The bulk crystalline Ge PV material has a bandgap of 0.66 eV, and a lattice constant almost perfectly matched to that of GaAs (0.566 nm for Ge and 0.565 nm for GaAs). The InGaP/GaAs/Ge 3J solar cells have realized conversion efficiencies of over 40% under concentrated 240-sun AM1.5d illumination with, and have been applied extensively to, space and terrestrial use [37].

Although Ge is well lattice matched to GaAs, it should be noted that a low-bandgap Ge bottom subcell in 3J solar cells produces approximately a current density ($>20\,\mathrm{mA/cm^2}$) much higher than the upper InGaP and GaAs subcells ($\sim14.5\,\mathrm{mA/cm^2}$), leading to non-ideal current matching [38]. As the output current of a MJ cell is limited by the subcell producing the lowest photocurrent, architectures that more closely balance the photocurrent among all subcells typically improve the efficiency. Furthermore, a more proper material with a larger bandgap could be a preferable choice, which could potentially lead to an increased open-circuit voltage.

6.2.3.2 InGaP/GaAs/InGaAs

As stated in the previous section, the triple junction InGaP/GaAs/Ge MJ solar cells have been widely used as a mature technique. However, the combination of subcell bandgaps in this design is not optimized for the solar spectrum. Therefore, a bottom subcell with an optimal bandgap needs to be further explored. Higher efficiencies can be obtained by optimizing the bandgaps of all three subcells, in which the Ge bottom junction could be replaced with a 1.0 eV junction $In_{0.3}Ga_{0.7}As$-based subcell. In a typical 3J cell architecture, the InGaP/GaAs/InGaAs structure is epitaxially grown by molecular beam epitaxy (MBE) or MOCVD methods in an inverted order: on a GaAs substrate, lattice-matched top InGaP and bottom GaAs subcells are grown at first, followed by transparent graded-composition buffer layers, and finally a metamorphic 1 eV InGaAs bottom cell [39, 40]. The GaAs substrate is subsequently removed via mechanical polishing and/or chemical wet etching and the thin-film device is bonded to a carrier substrate for the remaining processing steps. The reason to employ such an inverted cell structure is mainly attributed to the $\sim$2% lattice mismatch between InGaAs and GaAs. Such an inverted cell structure can ensure that the high-quality InGaP and GaAs cells are first fully lattice matched

grown on the GaAs substrates, with defects such as misfit dislocations only forming in the lastly grown InGaAs cell. Furthermore, this lattice matching presents the elastic strain property; a tunable bandgap energy can be achieved by shifts of the valence/conduction bands, heavy/light hole valence bands, or by inducing coupling between neighboring bands. So, these lattice-mismatched heterostructures exhibit a high flexibility in tailoring their electrical and optical properties, offering an additional degree of freedom to design the optimal bandgap configuration. It has been proved to offer an increased efficiency by the introduction of the lattice mismatch subcells in the 3J solar cells [41].

In 2013, Sasaki et al. have developed InGaP/GaAs/InGaAs MJ solar cells with an efficiency of 37.7% under AM1.5g illumination by improving the growth crystal quality and optimizing the cell structure. Meanwhile, Sharp Corporation obtained the highest monolithic InGaP/GaAs/InGaAs solar cell conversion efficiency of 44.4% within a lens-based concentrator system providing 302-sun illumination [42]. Because of their particularly high conversion efficiency and cost, such MJ compound solar cells have thus far been used primarily on space satellites.

6.2.3.3 InGaP/GaAs/InGaAsNSb

Lattice mismatch between GaAs and InGaAs cells causes challenges during the fabrication process, so designing a 1 eV bottom cell lattice matched to GaAs would be highly desirable for high-efficiency MJ solar cells. By introducing an InGaAsNSb (also called dilute nitride) material with a bandgap of 1 eV that is lattice matched to GaAs or Ge in the bottom cell design, the corresponding MJ solar cells could grow upright, eliminating complexities associated with growth strain and wafer bowing [43]. Wiemer et al. fabricated InGaP/GaAs/InGaAsNSb 3J cells with efficiencies of 43.5% under illumination of 400–600 suns, which maintained efficiencies above 43% under 1000-sun conditions [44].

6.3 Thin-Film III–V Solar Cells on Flexible Substrates

Conventional single and MJ III–V solar cells are usually not thin-film cells, as the cell structures are grown on thick GaAs or Ge wafers. These materials are typically direct-bandgap semiconductors with large optical absorption coefficients; thereby, thin films with thicknesses of only a few micrometers are sufficient to absorb photons with energies above their bandgaps. GaAs and Ge growth wafers are not only expensive but also mechanically rigid, thus preventing cost reduction and their further use in versatile applications. The main driving forces for innovation in PV research involve increasing the cell and module efficiencies as well as decreasing the system cost. One advantage of forming flexible III–V solar cells is related to significant cost saving by reusing the expensive growth substrates. In addition, some emerging application fields call for lightweight solar cells that can be integrated with flexible substrates and still maintain high efficiencies.

Many ingenious thin-film release methods, including the smart-cut [45], eltran [46], controlled spalling technology (CST) [47, 48], ELO [17, 49]

and their variants have been developed over the last few decades. These methods allow successful retrieval of thin-film semiconductor membranes from growth substrates and their transfer onto other substrates, enabling a variety of applications such as silicon-on-insulators (SOIs) for complementary metal-oxide-semiconductor (CMOS), 3D integration, optoelectronic devices, and flexible electronics [8, 48, 49]. In addition to the cost reduction associated with substrate recycling, freestanding thin-film III–V cells create new opportunities because of their flexibility and light weight. It will be beneficial for both terrestrial and space applications if III–V MJ solar cells can significantly reduce weight and be manufactured cost-effectively while maintaining their high efficiencies. Strategies to form thin-film released solar cells and their integration with heterogeneous substrates are overviewed and discussed in the following sections.

6.3.1 Mechanical Spalling

CST is based on a unique mode of brittle fracture whereby a surface layer with tensile stress induces fracture parallel to (and below) the film/substrate interface [47, 48]. It can be performed at room temperature using inexpensive laboratory equipment and applied at nearly any point in the semiconductor manufacturing process – from ingots to starting substrates to completed devices.

Figure 6.3a schematically illustrates the controlled spalling process [48, 52]. The key steps of this technology are (i) depositing a tensile stressor layer with a critical thickness, (ii) applying a flexible handle layer to the surface of the stressor, (iii) initiating a crack near the edge of the wafer, and (iv) mechanically guiding the fracture front across the substrate to release the semiconductor membranes. The origin of this spalling effect lies in a combination of two mode components for the pure opening and shear stress. As shown in Figure 6.3b, the formed crack prefers to propagate along the direction where the shear stress (K_{II}) is minimized. For a compressive layer, the crack deflects up and breaks the film. For a tensile layer, the crack deflects into the substrate at the depth where $K_{II} = 0$, forming a stable crack trajectory [47, 50, 51]. The stressor layer with a suitable thickness can be made of many different materials and formed by methods such as sputtering or electroplating. A commonly used stressing material is nickel (Ni), because of its low cost and controllable mechanical properties in the films.

In CST, the handle layer plays an important role by promoting pure spalling mode fracture while suppressing parasitic modes of fracture (such as channel mode fracture). However, since there is no spontaneous fracture, a crack must be introduced at the edge of the wafer. Because the spalled film/substrate combination forms a stressed bilayer, the semiconductor is capable of cracking if it is mishandled. Therefore, the handle layer also provides a convenient way to manipulate the thin semiconductor layer without introducing cracks [5, 48].

Operating at room temperature, the CST can be applied to kerf-free ingot dicing, removal of preformed p–n junctions or epitaxial layers, or even completed devices. Bedell et al. successfully demonstrated kerf-free ingot dicing, as well as the removal of III–V single junction epitaxial layers from a Ge substrate [47]. Shahrjerdi et al. reported ultralight flexible dual-junction InGaP/(In)GaAs
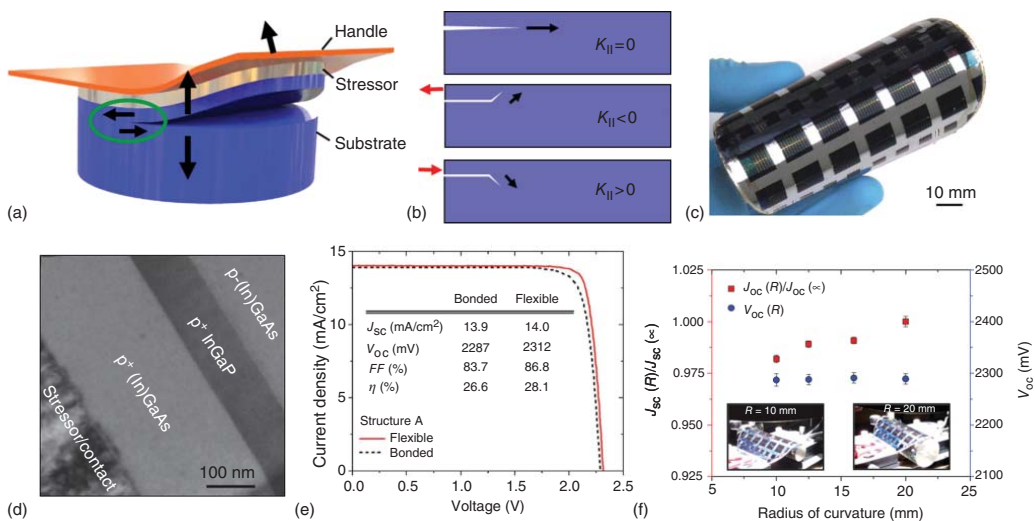
Figure 6.3 (a) Schematic illustration of the controlled spalling process. Source: https://creativecommons.org/licenses/by/3.0/, [48]. (b) Schematic illustration of the relation of the shear stress (K_{II}) and directions of the corresponding cracks [47, 50, 51]. (c) Photograph of the transferred flexible InGaP/(In)GaAs tandem solar cells on plastic substrate (diameter: 10 cm) after controlled spalling. (d) Cross-sectional transmission electron microscopy (TEM) image of the transferred thin film structure, indicating no visible defect after controlled spalling. (e) Current density–voltage curves for the transferred solar cells on a flexible substrate (red line) and on a Si wafer bonded using a silver-based conductive epoxy (black dotted line) under simulated AM1.5g illumination. (f) The stability of flexible InGaP/GaAs solar cells under bending at different radii of curvature. Source: Reproduced with permission from Shahrjerdi et al. [5]. Copyright 2013, John Wiley & Sons.

solar cells on plastics with a conversion efficiency of 28% by employing CST (Figure 6.3c). Solar cells formed on the spalled GaAs substrates and transferred on plastic substrate own characteristics similar to nonspalled (bulk) ones, indicating that the quality of the epitaxial layers is not compromised after spalling (Figure 6.3d,f). The released solar cells exhibit remarkably high specific power and excellent stability under different bending conditions (Figure 6.3e,f) [5]. In the fabrication scheme, the Ni stressor layer used for removing the solar cells structure from the growth wafer simultaneously functions as the backside ohmic contact. In addition, a thin polyimide tape was utilized as the flexible handle layer to further serve as the supporting substrate throughout the device fabrication process owing to its exceptional high-temperature stability. During the layer transfer process, it was demonstrated that the integrity of the entire device structure is maintained.

6.3.2 Epitaxial Lift-Off

ELO methods allow the separation of a III–V device structure from its grown substrate using selective wet etching of a thin sacrificial layer, as shown in Figure 6.4a, which was first reported by Konagai et al. in 1978 by separating a GaAs-based device layer from a GaAs substrate by using hydrofluoric acid (HF) to selectively etch a sacrificial AlGaAs layer inserted between the device film and the substrate during growth [54]. Subsequently, similar approaches have been applied by many researchers to successfully peel GaAs thin-film devices from the parent substrates and transfer them onto desirable substrates for various applications [10, 49, 55].

The basis of the ELO process relies on a thin sacrificial layer deposited on the wafer between the substrate and the thin-film device structure layer, which is typically 10–1000 nm $Al_xGa_{1-x}As$ (with $x > 0.6$, mostly x is taken as 1 to be AlAs) for GaAs- and InGaP-based optoelectronic devices. In the $Al_xGa_{1-x}As$ film, increasing the fraction of Al results in significantly enhanced etching rates in HF. Since $Al_xGa_{1-x}As$ has a lattice constant that is almost identical to GaAs, only a minimal additional lattice misfit strain is introduced during growth and the perfect single crystal structure in the active device layer can be maintained. During the ELO process, the sacrificial $Al_xGa_{1-x}As$ layer is removed by wet chemical etching in an HF solution, while keeping the other cell structures free of damage. Based on selective removal of the sacrificial layer, we could separate the thin epitaxial wafer from the growth substrates (top, Figure 6.4c).

In the past few years, companies such as Alta Devices [8] and Microlink Devices [56, 57] have developed a wafer-scale, ELO manufacturing process and are currently in pilot production. For the removal process of sacrificial layers, wet chemical etchants are typically used [10]. Conventionally, a low-concentration HF solution is needed to etch the thin AlAs layers, because otherwise the hydrogen produced during the etching process can form gas bubbles, resulting in cracks in the layer structure and blocking the etching channel (Figure 6.4b).
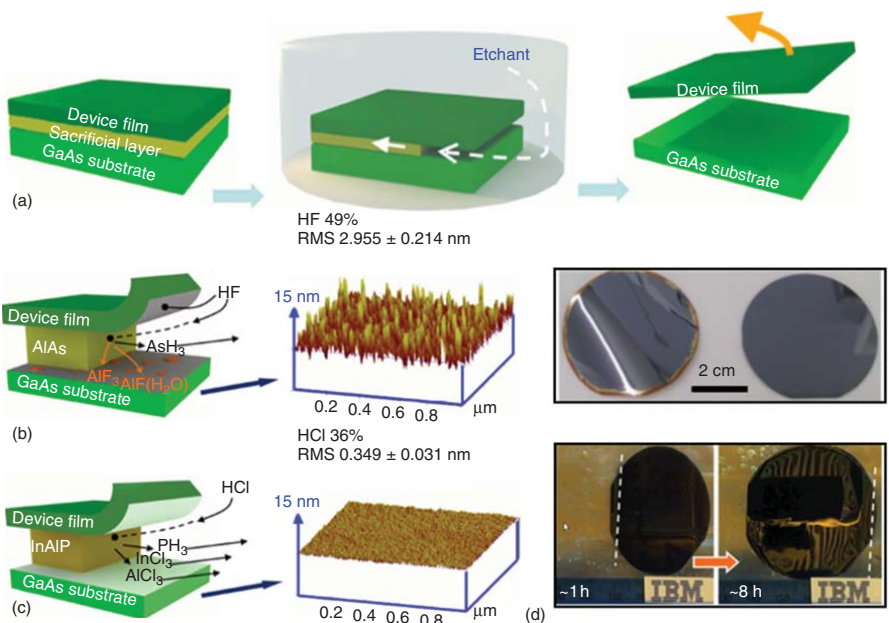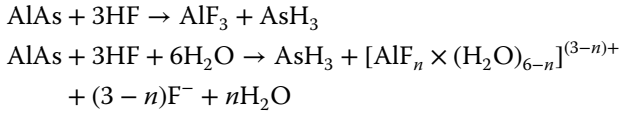
Figure 6.4 (a) Schematic illustration of epitaxial lift-off (ELO) process [10]. The chemical reactions near the interface of different sacrificial layers, e.g. (b) AlAs, (c) InAlP, and etchants e.g. (b) HF, (c) HCl, as well as the corresponding atomic force microscopy (AFM) images of the substrate surfaces after the lift-off process. Source: Reproduced with permission from Cheng et al. [10]. Copyright 2013, Nature Publishing Group. (d) Photographs of the released layers on the new substrates and parent substrates after the ELO process [10, 58].

The reaction of AlAs with an aqueous HF solution can be described by the following set of overall reactions:

$$AlAs + 3HF \rightarrow AlF_3 + AsH_3$$
$$AlAs + 3HF + 6H_2O \rightarrow AsH_3 + [AlF_n \times (H_2O)_{6-n}]^{(3-n)+}$$
$$+ (3-n)F^- + nH_2O$$

Three primary by-products from the etching reactions are AlF_3, $[AlF_n \cdot (H_2O)_{6-n}]^{(3-n)+}$, and AsH_3. AsH_3 is gaseous and can form bubbles and diffuse away from the interface to the solvent. These primary solid by-products of AlF_3 and $[AlF_n \cdot (H_2O)_{6-n}]^{(3-n)+}$ are hard to be dissolved into the solution. In addition, solid As_2O_3 can also be generated during the etch process according to the oxygen concentration of the etchant [10, 58, 59].

Yoon et al. fabricated GaAs optoelectronic devices including solar cells, transistors, and infrared imagers by using the releasable GaAs/AlAs multilayers with the ELO and transfer printing technique shown in Figure 6.5a−d [49]. Via these approaches, devices made of compound semiconductors such as GaAs can be fabricated and implemented in applications that are incompatible with conventional growth or integration strategies, in term of their cost structures, formats, area coverages and/or modes of use. However, one challenge associated with the HF-based etchant is the damages to the vulnerable p-ohmic contact, resulting in restrictions on the transfer implementation for the n-on-p structure. To address this issue, Moon et al. proposed a new low-resistivity p-ohmic metal that could withstand the HF etching in the ELO process [58].

As shown in Figure 6.4c, another ELO process with a sacrificial layer made of phosphide-based materials and the hydrochloric acid (HCl) etchant can be applied to selective etching, avoiding the insoluble etching by-products generated on the substrate surface [10, 60]. For example, phosphide-based materials (InGaP, InAlP, InP, etc.) have been widely applied as etch stop layers for the selective etching of arsenide-based materials (GaAs, InGaAs, etc.), and vice versa. It is known that HCl-based solutions can etch phosphide-based materials:

$$InXP + HCl \rightarrow InCl_3 + XCl_3 + PH_3$$

X could be Al or Ga; the gaseous PH_3 diffuses away from the interface and the rest of the etching by-products are highly soluble; thus, no residues are left on the wafer surface. This uniqueness stems from the perfect etch selectivity between GaAs and phosphides within the HCl etchant. Cheng et al. enhanced the throughput of this ELO process in a surface tension-assisted (STA) method, in which the wafer was placed obliquely with an angle (θ) of 1−20° from the etchant solution surface, and HCl was added to the level of the etching front [10]. During the STA-ELO process, the film was pulled by the surface tension away from the substrate and flattened on the surface of the etchant. In the meantime, the HCl etchant fills the gap between the GaAs substrate and the released device film via capillary action, sustaining the reaction process (bottom, Figure 6.4c) [10].

In addition, other strategies for interlayers have also been explored to facilitate the epitaxial release process. For example, Kim et al. introduced a graphene assisted "remote" homoepitaxy method shown in Figure 6.5e. Before depositing
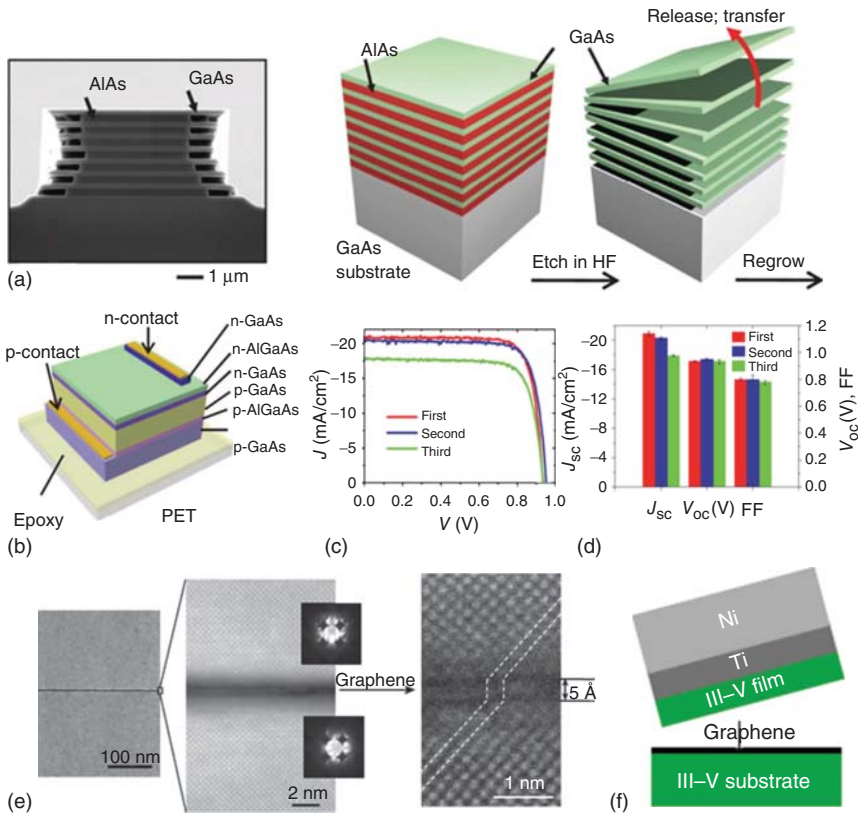
Figure 6.5 (a) Scanning electron microscopy (SEM) image and schematic illustrations of a multilayer stack of GaAs/AlAs and epitaxial lift-off (ELO) process by selective etching of the AlAs layers. (b) Schematic illustration of GaAs single junction solar cells on a polyethylene terephthalate (PET) substrate, where the single junction solar cells are epitaxially grown in trilayer assemblies separated by sacrificial layers of AlAs. (c) The current density–voltage curves for the three individual solar cells under AM1.5d illumination measured on the source wafer with an antireflection coating layer of Si_3N_4, and (d) the short-circuit current density, open-circuit voltage, and fill factor of the three solar cells. Source: Reproduced with permission from Yoon et al. [49]. Copyright 2010, Nature Publishing Group. (e) Scanning transmission electron microscopy (STEM) images of GaAs grown on the monolayer graphene–GaAs substrate with excellent remote alignment. (f) Schematic illustration of epitaxy lift-off process for the single-crystalline III–V films exfoliated from graphene–III–V substrate. Source: Reproduced with permission from Kim et al. [53]. Copyright 2017, Nature Publishing Group.

active device layers, a graphene monolayer was applied on III–V substrates, without disrupting the continuity of lattice-matched epi-growth. The inserted graphene monolayer significantly reduced mechanical bonding between the grown III–V layers and substrates; thereby, the thin-film devices can be easily exfoliated (Figure 6.5f) [53]. Such approaches have been applied to GaAs, InP, GaP, and GaN based materials. Being separated from the brittle and bulky substrates, highly bendable thin-film III–V devices such as LEDs and solar cells are formed.

6.3.3 Mechanical Designs

By taking advantage of various epitaxial releasable methods, thin-film semiconductor membranes and devices can be realized by replacing rigid bulky growth substrates with thin-film supporting materials (such as organics), enabling unusual light weight, flexibility, stretchability, and even biocompatibility. With the aid of heterogeneous integration of inorganic devices and organic substrates, as well as unique mechanical design concepts, highly flexible and stretchable solar cells and modules are achieved.

Yoon et al. fabricated large-scale single crystalline Si-based thin-film microcell arrays from bulk (111) Si wafers and integrated them on flexible substrates via the transfer printing technique [61]. The resulting microcell array systems offer high mechanical flexibility. Similarly, III–V solar cells could also be transferred and combined with various organic substrates such as polyimide or polydimethylsiloxane (PDMS), forming mechanically flexible and even stretchable electronic/optoelectronic systems. Lee et al. reported mechanical designs to form highly stretchable solar modules that use ultrathin, single junction GaAs solar cells and dual-junction InGaP/GaAs cells, respectively shown in Figure 6.6a,b
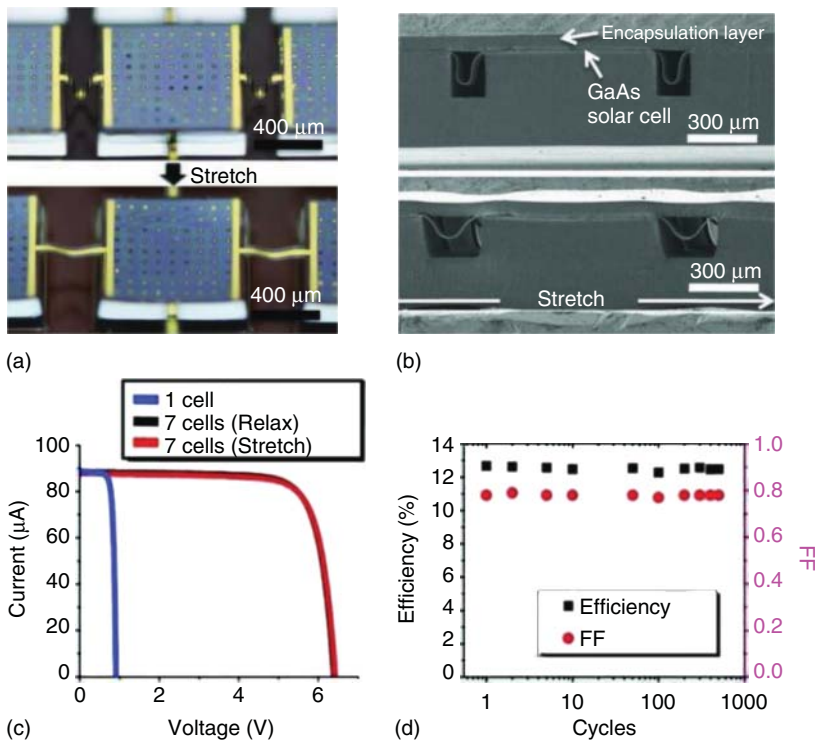

Figure 6.6 (a) Optical images (b) and SEM cross-sectional images of the GaAs solar cells in relaxed and stretched states. (c) The current density–voltage curves for a single microscale solar cell and seven cells connected in series in relaxed and stretched states. (d) Stability of the mechanical cycling tests for the interconnected microscale solar cells. Source: Reproduced with permission from Lee et al. [62]. Copyright 2011, John Wiley & Sons.

[62, 63]. In these platforms, PDMS-based elastomeric substrates are mechanically designed, including surface relief regions that confine strains at specific interconnected places away from the microcells. The performance of the solar cell arrays was unchanged under a biaxial strain up to 20% in the cycling test (Figure 6.6c,d). This stretchable and high areal coverage system presented a naturally formed strain-limiting behavior, in order to avoid destructive effects of extreme deformations.

6.3.4 Microcells with Luminescent Solar Concentrators

Luminescent solar concentrators (LSCs) utilize wavelength shifting luminophores including phosphors, luminescent dyes, and quantum dots (QDs), which are embedded in the transparent glass sheets or polymeric waveguides, to absorb part of the sunlight and re-emit light at other wavelengths that can then be concentrated onto the surfaces of small-scale solar cells. With LSC designs, photocurrents of solar cells could be significantly increased, in proportion to solar concentration. Meanwhile, higher open-circuit voltages (V_{oc}) are obtained, as well as increased efficiencies [64–66]. Unlike conventional concentrators that require complicated trackers and are inefficient to capture diffuse light, LSCs overcome the fundamental etendue limit by downshifting the wavelengths of incident light, thus eliminating the need for trackers, accepting sunlight from all the angles and potentially being able to obtain ultrahigh concentration ratios [67]. Yoon et al. designed ultrathin, flexible LSCs with embedded Si microscale solar cells (dimensions of $50\,\mu m \times 24\,\mu m \times 15\,\mu m$), in which the photons emitted could be guided into the side and bottom surfaces of the Si cells, resulting in a >300% output power enhancement [66]. Compared to the conventional LSC layout with bulky architectures, this LSC design (Figure 6.7a) offered improved performance by accepting the sunlight onto all-around surfaces for the embedded micro Si solar cells. Additionally, systematic studies on the LSC structural parameters are performed to reveal the light concentration mechanism of the LSCs (Figure 6.7b,c).

LSCs based on different optical designs could offer various levels of concentration by focusing diffuse light. In order to reduce waveguide loss leakages, various surrounding materials with different refractive indexes for LSCs were studied [69]. Sheng et al. transferred thin-film, microscale GaAs solar cells and arrays printed onto LSC waveguides, achieving a more than doubled power output (Figure 6.7d) [68, 70]. Carefully designed GaAs thin-film solar cells exhibit bifacial responses, receiving photons from both front and back surfaces. With optimized LSCs surrounded by air and an underlying diffuse reflector, both waveguided and scattered photons were captured (Figure 6.7e). With the ELO and transfer printing techniques, such LSC-integrated microscale III–V solar cells and modules provide a routine for further scale-up module production.

Alternatively, QD-based LSCs are of great interest due to their superior stability under long-term sunlight exposure [71, 72]. QDs with large Stocks shift, near-field energy transfer, and phosphorescence properties could potentially reduce the spectral overlap of absorbed/emitted photons, thereby reducing the reabsorption of luminescence in LSCs [69, 73–75]. Bronstein et al. designed
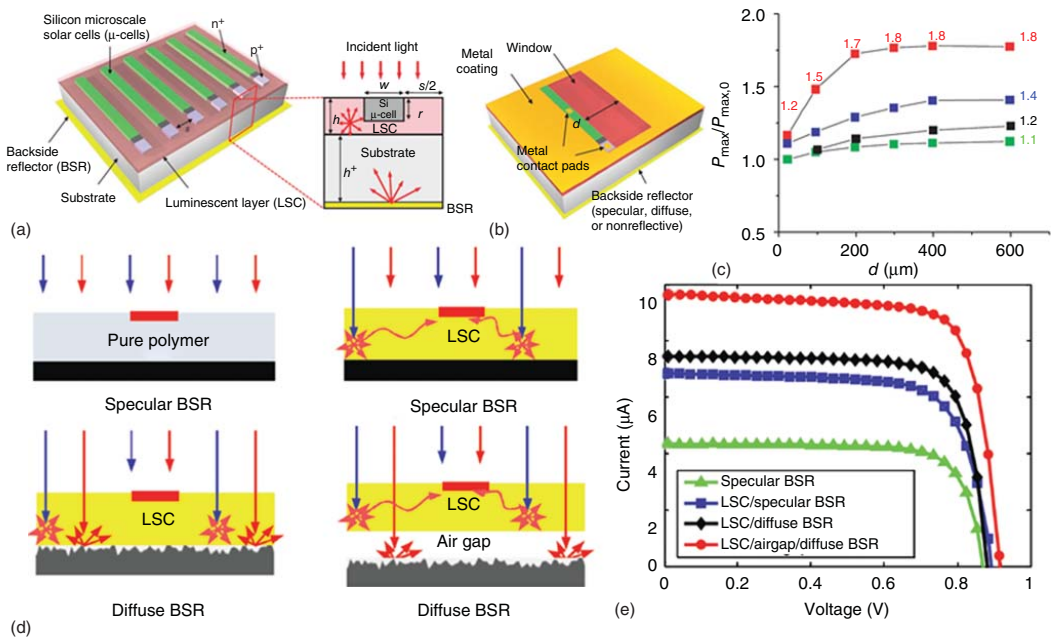
Figure 6.7 (a) Schematic illustration of the luminescent concentrators (LSCs) layer assisted by an array of microscale solar cells, with a transparent glass substrate on a backside reflector (BSR). The inset shows the key parameters of the PV system in a cross-sectional view. (b) Schematic illustration of solar cells embedded in LSC systems with variable illumination area by changing the aperture width (d) and three different BSRs. (c) The corresponding normalized maximum output power ($P_{max}/P_{max,0}$) of solar cells as a function of the aperture width of the design with LSC with different BSRs, which are nonreflective (green), specular- (red) and diffuse-reflective (blue) BSRs, and without LSC with diffuse-reflective BSR (black). Source: Reproduced with permission from Yoon et al. [66]. Copyright 2011, Nature Publishing Group. (d) Schematic illustrations of GaAs microscale cells embedded on LSC waveguides with different surroundings and BSRs, (e) and the corresponding measured current–voltage curves under AM1.5g illumination. Source: Reproduced with permission from Sheng et al. [68]. Copyright 2013, John Wiley & Sons.

LSCs with a combination of nanocrystal lumophores (CdSe/CdS QDs) and photonic cavities to trap the emitted photons [76]. The optical cavity was formed by coupling a photonic mirror with a luminescent waveguide, resulting in omnidirectionally trapped emitted luminescence. By mitigating scattering losses and minimizing the escape cone, the LSCs offered a concentration ratio over 30 while maintaining a waveguide efficiency of 82%. Eventually, this design provided a potentially low-cost and high-performance alternative to costly high-bandgap III–V semiconductor materials to serve as a top junction in MJ PV devices for efficient utilization of blue photons.

6.4 Applications

The continuously increased conversion efficiency of III–V solar cells in recent years can be attributed to developments in high-quality semiconductor materials and devices, as well as advanced electronic and optical designs (e.g. inverted metamorphic growth, wafer bonding, mechanical stacking, and LSCs). Combining with emerging techniques such as controlled spalling and ELO, thin-film inorganic solar cells can be separated from the expensive growth substrate, allowing substrate reuse. Meanwhile, the released thin-film devices can be transferred onto new substrates, such as flexible and stretchable sheets, enabling novel functionalities via heterogeneous integration. Because of their significantly reduced weight, high conversion efficiency, excellent stability, and unique mechanical properties, flexible III–V solar cells have been applied to many domains, including space, aircraft, and life sciences.

Outer space is a harsh environment. Its characteristics of high vacuum, intense radiations, temperature cycling, etc. bring additional design challenges for solar cell implementations [11]. Since the first solar-powered satellite Vanguard I (Figure 6.8a) was launched in 1958 (https://nssdc.gsfc.nasa.gov/nmc/spacecraftDisplay.do?id=1958-002B), solar cells have become the most used power supply for space applications. It should be noted that efficiencies of space solar cells are measured and operated under the extraterrestrial reference spectrum AM0 ($1347.9 \, \text{W/m}^2$), different from the terrestrial solar spectrum AM1.5g ($1000.4 \, \text{W/m}^2$) (http://rredc.nrel.gov/solar/spectra/am1.5/). Compared to the solar technology with Si cells that has been used on many of the preceding satellites, III–V solar cells have higher ascendancy due to many of their own characteristics: e.g. more robust adaptation to radiation in space environment, high conversion efficiencies, and extremely low performance degradation with temperature changes. Additionally, high optical absorption coefficients of direct-bandgap III–V semiconductors lead to thin-film PV cells with high power per weight. Efficiencies of MJ III–V solar cells for space uses reach more than 30% for InGaP/GaAs/Ge 3J cells and as high as 38.8% for 5J cells (2.2/1.7/1.4/1.05/0.73 eV), under the AM0 condition [79]. As the efficiencies of III–V MJ solar cells and panels approach more than 30%, they become more and more attractive for implementation onto many satellites and space vehicles [1, 80].
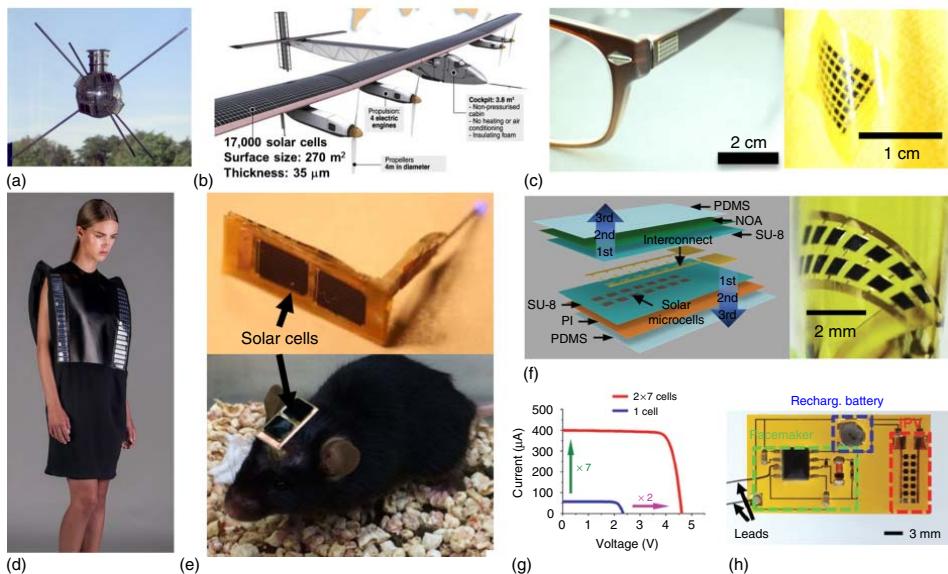
Figure 6.8 (a) Vanguard I satellite (https://nssdc.gsfc.nasa.gov/nmc/spacecraftDisplay.do?id=1958-002B). (b) The new solar-powered aircraft of Solar Impulse 2 (http://www.solarimpulse.com/). (c) Optical images of flexible thin-film solar cells integrated onto the frame of glasses (left) and fabric (right). Source: Reproduced with permission from Kim et al. [77]. Copyright 2016, AIP Publishing LLC. (d) A prototyped costume made of wool and leather integrated with solar cells (http://www.paulinevandongen.nl/project/wearable-solar/). (e) Photographs of the solar powered harvesters (top), including the solar cells, LED and RF control logic, and the implantation (bottom) in the head of behaving mice. Source: Reproduced with permission from Park et al. [78]. Copyright 2015, IOP Publishing. (f) Schematic illustration of implantable microscale PV cells and the image of the fabricated solar cells on a flexible substrate, (g) current–voltage curves for an individual PV cell and interconnected microcells. (h) Optical image of a flexible cardiac pacemaker integrated with the implantable devices (shown in f) and a rechargeable battery, (i) and the implantation in a living mouse (left), where the right photograph shows the leads from the implanted self-powered pacemaker contacting the right atrium (RA) and left ventricle (LV) of the heart. (j) Output impulses (3 Hz) from the subdermally implanted self-powered pacemaker powered by the inorganic photovoltaic (IPV) devices under AM1.5g illumination, and powered by the stored energy without illumination. Source: Reproduced with permission from Song et al. [12]. Copyright 2016, John Wiley & Sons.
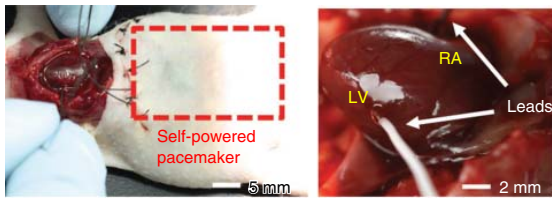
(i)
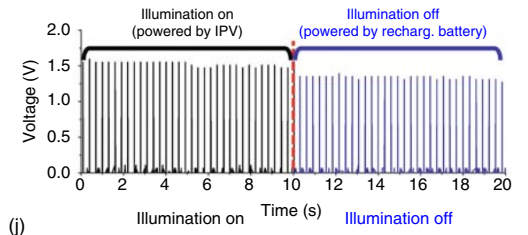
(j)

Figure 6.8 (*Continued*)

With increasing demand for an aircraft that can operate away from large airports and fuel supplies, solar powered air vehicles would be an ideal solution (https://www.nasa.gov/centers/armstrong/news/FactSheets/FS-054-DFRC .html). In 2015–2016, a solar aircraft named Solar Impulse 2 started circumnavigation of the Earth (Figure 6.8b), which achieved the longest solo solar flight of ~40 000 km (http://www.solarimpulse.com/). If the monocrystalline Si solar panels in this aircraft are replaced with high-efficiency thin-film III–V MJ solar cells, a longer cruise time, faster and better carrying capacity aircraft can be achieved with the extra high power supply and less weight.

Flexible and lightweight thin-film solar cells have attracted considerable attention for their potential uses as portable electronic chargers, bendable display devices, and wearable electronic textiles, on account of their comfort, convenience, and versatile functionality (Figure 6.8c) [81]. Dogen et al. designed a prototyped costume made of wool and leather integrated with 48 rigid solar cells on the coat and 72 flexible solar cells on the dress (Figure 6.8d) (http:// www.paulinevandongen.nl/project/wearable-solar/). Under sunlight, a typical smartphone can be charged by about 50% in one hour.

Nowadays, the demand for implantable medical devices and systems is also greatly increased, associated with factors including the increasing aging/baby boomer population, chronic degenerative diseases with ineffective pharmacological treatments, congenital diseases, etc. (http://www .todaysmedicaldevelopments.com/article/global-implantable-medical-device-market-2024-31517/). Although the performance and functionality of the implantable devices are being improved and extended, the electrical capacities of most implants are limited by integrated batteries. Replacement procedure is required when the battery is depleted, causing risks of medical complications for patients. The employment of integrated solar cells to drive or recharge implanted electronic medical devices provides a viable solution for power delivery in medical devices.

To acquire and analyze the data of received power after the implantation as time goes on, Bereuter et al. used subcutaneous solar cells monitored by portable light measurement to analyze the real-life validation data of energy harvesting in different seasons [82]. Park et al. designed a wireless control/harvesting system using radio frequency (RF) control with InGaP/GaAs PV cell-based energy harvesters [78]. With lightweight 2J solar cells, the wireless RF signal coverage was greatly enhanced. Combined with injectable microscale inorganic LEDs, such an energy supply platform offered versatile capabilities in optogenetics by modulating light signals in the brain region of freely behaving animals (Figure 6.8e). This solar harvester was still placed outside the tissue, while fully implanted devices could be more attractive for some specific clinical research. Song et al. designed an implantable solar energy harvester by using flexible, ultrathin, and high-efficiency InGaP/GaAs 2J solar cells (Figure 6.8f–h), which could be transfer-assembled and encapsulated with biocompatible materials for subdermal electricity generation [12]. Because of its small size, the implantation procedure only required a simple dermatological surgery. These high-performance, flexible III–V cell arrays generate sufficient power to operate implanted devices such as electronic sensors and light emitters (Figure 6.8i,j).

6.5   Future Generations

6.5.1   More Junctions

MJ solar cells achieve much higher conversion efficiency than single junction cells, mainly due to the efficient use of the broadband solar spectrum by subcells with different bandgaps. Double and triple junction III–V solar cells are applied in standard PV modules for industrial applications, among which the state-of-the-art inverted metamorphic InGaP/GaAs/InGaAs 3J solar cells achieved an efficiency record up to 44.4% [42, 83]. In order to fully utilize the solar spectrum, III–V solar cells with 4J, 5J, and even more junctions are being actively investigated to reach even higher efficiencies.

Theoretically, more junctions generally offer higher conversion efficiencies for MJ solar cells. However, challenges associated with combination of materials need to be considered, including material growth quality, lattice constant, bandgap, absorption coefficient, mobility, minority carrier lifetime, and availability of suitable barrier materials [84, 85]. For example, InGaP/GaAs/InGaNAs/Ge 4J cells are derived from the InGaP/GaAs/Ge 3J cells by insertion of an InGaNAs junction, which is lattice matched to GaAs and can be grown by MBE or MOCVD methods. However, the poor minority carrier transport in InGaNAs layers causes lower photogenerated currents and voltages than theoretical predictions [86, 87]. Five- and six-junction (5J and 6J) solar cells have been proposed to realize more than 50% conversion efficiencies. King et al. designed fully lattice-matched (Al)InGaP/InGaP/Al(In)GaAs/(In)GaAs/InGaNAs/Ge 6J solar cells with corresponding bandgaps of 2.00/1.78/1.50/1.22/0.98/0.67 eV [88]. However, such devices with high efficiencies have not been experimentally realized due to the daunting challenges related to monolithic growth and fabrication.

6.5.2   Mechanical Stack

Alternatively, lattice-mismatched MJ cells with optimum bandgap combinations formed by mechanical stacking overcome challenges such as lattice and current matching associated with the epitaxial growth mentioned above [88, 89]. Zhao et al. designed GaAs//Ge mechanical 2J solar cells with a conversion efficiency of 27.2% at 1-sun and 32.1% at 30-sun AM1.5d illumination, and it could be easily extended to the InGaP/GaAs//Ge 3J solar cells [90]. Thus, current matching issues can be solved in MJ solar cells and the performance is only limited by the series resistance instead of the intrinsic properties of the cells. Sheng et al. realized 4J, four-terminal InGaP/GaAs/InGaAsNSb//Ge MJ solar cells by introducing a stick interlayer of As_2Se_3 via sol–gel process (Figure 6.9a–d), the measured efficiency of which was 43.9% at concentrated 1000-sun condition, and the efficiency of the modules was up to 36.5% [91]. Chiu et al. fabricated 5J cells with the bandgap of 2.2/1.7/1.4/1.05/0.73 eV, the top 3J cells of which are grown on GaAs and the bottom 2J cells are grown on InP. Owing to the low temperature for the direct bonding of InP and GaAs cells, the proprietary process offered an increased mechanical yield and reduced large void density, with an efficiency
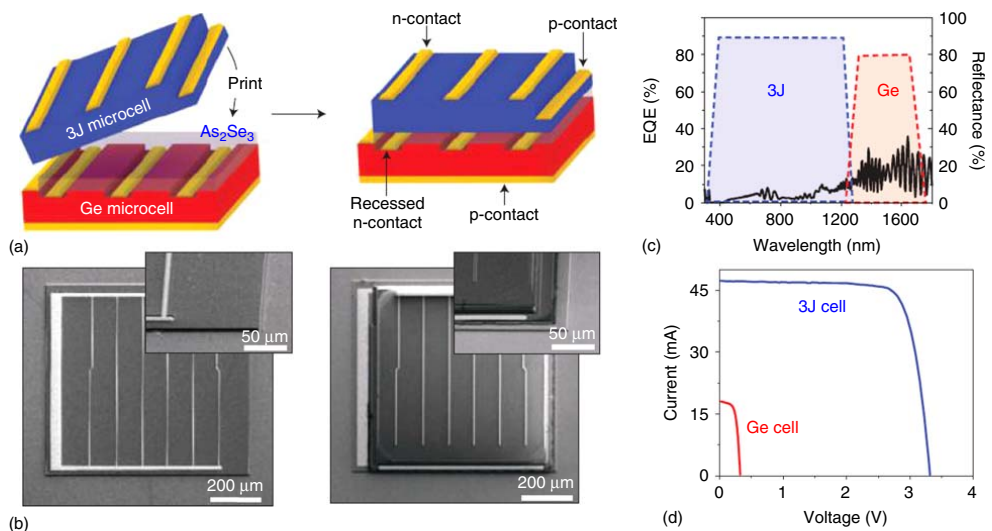
Figure 6.9 (a) Schematic illustrations (b) and SEM images of the 3J InGaP/GaAs/InGaAsNSb thin-film stack before (left) and after (right) transferred printing on a single junction Ge cell, with the interface layer of As_2Se_3 (light blue) providing excellent optical, electrical, and thermal properties. (c) Schematic illustrations of the EQE and measured reflectance spectra of the 3J/Ge cell. (d) Measured current–voltage curves for the module under direct exposure to sunlight. Source: Reproduced with permission from Sheng et al. [91]. Copyright 2014, Nature Publishing Group. (e) Schematic illustration of four-terminal GaInP/GaAs//Si triple-junction solar cells, where the top InGaP and middle GaAs cells are connected via a tunnel junction and stacked on a Si heterojunction solar cells. (f) EQE of the three subcells (g) and the current density–voltage curves for subcells and tandem cells under AM1.5g illumination. Source: Reproduced with permission from Essig et al. [55]. Copyright 2017, Nature Publishing Group.

(e)

GaInP/GaAs//Si triple-junction solar cell
ZnS/MgF$_2$ ARC
Front metal grid
n-GaAs contact

n-AlInP window
n-GaInP
p-AlGaInP back surface field
p/n AlGaAs tunnel diode
n-GaInP back surface field
n-GaAs
p-GaAs
p-GaInP back surface field
p-AlGaAs contact layer

Rear metal
ZnS ARC
Adhesive

Rear metal
ZnS ARC
Adhesive

Glass slide

Adhesive
Front metal

TCO
(p/i) a-Si:H
n-Si wafer (FZ)
(i/n) a-Si:H
TCO
Back metal

(f)

EQE (%) vs Wavelength (nm)

GaInP top cell
J_{photo} = 14.1 mA/cm^2

GaAs middle cell
J_{photo} = 13.5 mA/cm^2

Si bottom cell
J_{photo} = 11.1 mA/cm^2

(g)

Current density (mA/cm^2) vs Voltage (V)

Independent (four-terminal) operation:
GaInP/GaAs 2J top cell
SHJ bottom cell
Series connection of all subcells:
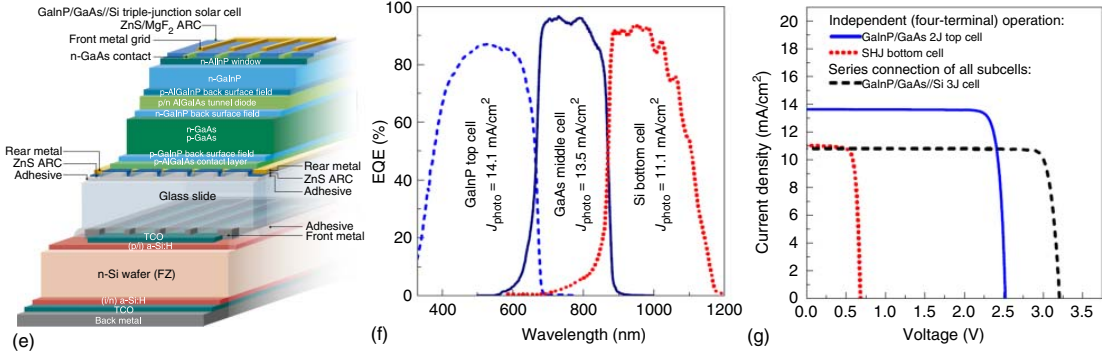GaInP/GaAs//Si 3J cell

Figure 6.9 (*Continued*)

of 35.1% under standard AM0 irradiation for the space application and 37.8% under AM1.5g irradiation for the terrestrial application [79]. Recent efficiency records were set by wafer bonded InGaP/GaAs//InGaAsP/InGaAs 4J solar cells with efficiencies up to 46.1% under 312-sun AM1.5d illumination [84]. Furthermore, other 4J architectures based on InP, Ge, or GaSb bottom cells were proposed with theoretical efficiencies of more than 50% [85, 92].

Combining III–V compounds with other semiconductor materials has been widely explored for different optoelectronic applications, in order to further decrease production costs, add new functions, and increase cell efficiencies [93–95]. Integrating high-efficiency III–V MJ solar cells on Si-based cell or substrate, which could achieve better performance and reduced cost, has attracted immense interest (Figure 6.9e). Essig et al. fabricated III–V//Si MJ solar cells via adhesive bonding, including the architectures of GaAs//Si, InGaP//Si and InGaP/GaAs//Si, achieving efficiencies of 32.8%, 32.5%, and 35.9% under AM1.5g illumination, respectively (Figure 6.9f,g) [55]. Compared to the theoretical 29.4% efficiency of conventional Si technology and the record InGaP/GaAs 2J solar cells with 32.6% efficiency, Si-based MJ III–V solar cells show great potential in the future.

6.5.3 Spectral Splitting

Splitting and absorbing the solar spectrum with MJ solar cells is considered to be an effective method to overcome the SQ limit and realize high conversion efficiency [13]. As introduced previously, the vertical MJ solar cells based on monolithic or mechanical concepts are widely used. Alternatively, the laterally arranged MJ solar cells with spectrum splitting and concentration architectures have also attracted significant attention. As shown in Figure 6.10a, spectral splitting elements redirect light with different wavelengths onto individual subcells with corresponding bandgaps. As an example, Xiong et al. designed a spectral splitting system with dichroic mirrors to separate the sunlight into two bands, which were then absorbed by two 2J solar cells (InGaP/GaAs and InGaAsP/InGaAs) respectively (Figure 6.10b) [96, 98].

Recently, advanced photon managements based on the wavelength scale compact structures have been explored to realize deterministic and efficient spectrum splitting and concentrating [99, 100]. Based on the principle of diffractive optics, Huang et al. fabricated a single thin planar diffractive optical element (DOE) shown in Figure 6.10c,d, in order to simultaneously split and concentrate the incident sunlight into several different spectral bands for lateral MJ solar cells [97].

6.5.4 Photon Recycling

Detailed balance theories determine that solar cell efficiency is highly correlated to the light emitting efficiency of the semiconductor diode, exemplified by the mantra "a good solar cell should also be a good LED" [101]. In other words, optimized materials quality and device structures lead to increased carrier lifetimes and enhanced radiative emission via electron–hole recombination from
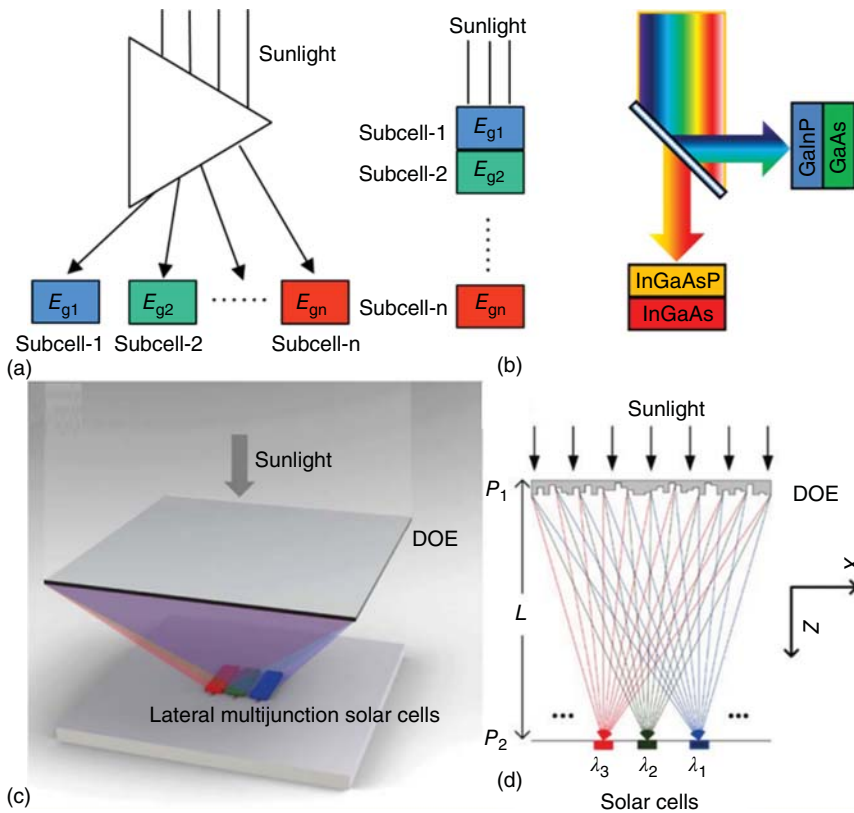
Figure 6.10 (a) Schematic illustrations of spectrum splitting in multijunction (MJ) solar cells, including the lateral (left) and vertical arrangements (right). (b) Schematic illustration of non-concentrating photovoltaic receiver with a dichroic mirror that splits the sun spectrum into two bands, and each part is separated again in the tandem cells resulting in conversion of light in four regions. Source: Reproduced with permission from Xiong et al. [96]. Copyright 2010, Elsevier Ltd. (c) Schematic illustration (d) and the profile view of lateral MJ solar cells with spectrum splitting solar concentrator based on diffractive optical element (DOE) architecture. Source: Reproduced with permission from Huang et al. [97]. Copyright 2013, Optical Society of America.

the device surface, thereby improving the open-circuit voltage and cell efficiency (Figure 6.11a) [102].

Recently, Alta Devices Inc. achieved a certified world-record efficiency of 28.8% for single junction GaAs solar cells under AM1.5g illumination by enhanced photon recycling design with a highly reflective mirror at the rear surface [8]. García et al. implemented an Al_2O_3-based reflector simply created by lateral oxidation of an AlAs layer in the GaAs solar cells, showing an increase of V_{oc} up to 18 mV. With analysis of different rear reflectors, the relation of the photon recycling effect and the refractive index of the backside reflector (BSR) was discovered [103]. Sheng et al. presented MJ solar cell architectures with improved photon recycling. Instead of using metallic reflectors, this design involves low refractive index materials (air, SU-8 photoresist) as angular and
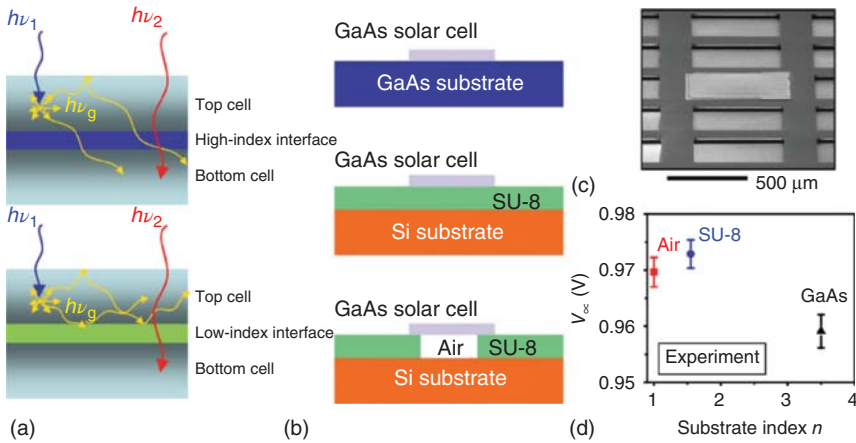
Figure 6.11 (a) Schematic illustrations of photon dynamics in multijunction (MJ) solar cells with a high- (top) or low-index (bottom) interface. (b) Schematic illustrations of GaAs DH solar cell on substrates with different interface materials. (c) SEM image of the GaAs solar cell printed on patterned SU-8 with interface of a 25 μm air gap. (d) Measured open-circuit voltage of microscale GaAs solar cells on substrates with different interface materials. Source: Reproduced with permission from Sheng et al. [70]. Copyright 2015, John Wiley & Sons.

wavelength selective bandpass interfaces between different subcells in the MJ structures (Figure 6.11b,c), ensuring that the top cell recycles and re-emits more luminescent photons to obtain higher photovoltages (Figure 6.11d) [70].

6.6 Conclusion

In this chapter, high-performance thin-film single junction and MJ III–V solar cells are reviewed. Employing advanced release methods such as controlled spalling or ELO, thin-film devices can be released and separated from growth substrates and integrated with lightweight flexible substrates. Their formation and integration strategies onto heterogeneous substrates are discussed not only as versatile options for solar energy harvesting in the terrestrial or space environment, but also as promising solutions to advanced wearable and portable systems with example applications in healthcare. So far, monolithically grown 3J III–V cells have reached a record efficiency of 44.4% under concentration (InGaP/GaAs/InGaAs cell by Sharp [42]), and further efficiency improvements would require more (>3) junctions that are difficult to grow monolithically and realize both lattice matching and current matching. Emerging concepts such as spectral splitting, luminescent concentrators, and photon recycling and the corresponding fabrication and integration processes are proposed to further enhance the photon conversion efficiencies and approach theoretical limits.

Because of their excellent performances and recently developed fabrication schemes, III–V based thin-film solar cells could potentially provide a viable solution to cost-effective electricity generation. By taking advantage of their high efficiencies, light weight and convenient uses, thin-film microscale III–V solar cells

and arrays on flexible substrates will serve as a high-performance remote power supply for our daily uses. Cell modules can be integrated with costumes, automobiles, buildings, aircraft, satellites, etc. On the other hand, the microscale PV cells will find applications in miniaturized systems, for example, being integrated with integrated circuits comprising batteries, sensors, transistors, and actuators for multifunctional sensing, diagnosis, and therapy in biomedicine.

References

1 Green, M.A., Hishikawa, Y., Warta, W. et al. (2017). *Progress in Photovoltaics: Research and Applications* 25: 668–676.

2 Nowak, S. (2016). Trends 2016 in Photovoltaic Applications: Survey Report of Selected IEA Countries Between 1992 and 2015. *Report IEA-PVPS.*

3 Powell, D.M., Fu, R., Horowitz, K. et al. (2015). *Energy & Environmental Science* 8: 3395–3408.

4 Singh, G.K. (2013). *Energy* 53: 1–13.

5 Shahrjerdi, D., Bedell, S.W., Bayram, C. et al. (2013). *Advanced Energy Materials* 3: 566–571.

6 Pagliaro, M., Ciriminna, R., and Palmisano, G. (2008). *ChemSusChem* 1: 880–891.

7 Sheng, X., Corcoran, C.J., He, J.W. et al. (2013). *Physical Chemistry Chemical Physics* 15: 20434–20437.

8 Kayes, B.M., Zhang, L., Ding, I.K., and Higashi, G.S. (2014). *IEEE Journal of Photovoltaics* 4: 729–733.

9 Rogers, J.A., Someya, T., and Huang, Y.G. (2010). *Science* 327: 1603–1607.

10 Cheng, C.W., Shiu, K.T., Li, N. et al. (2013). *Nature Communications* 4.

11 van Leest, R.H., Mulder, P., Gruginskie, N. et al. (2017). *IEEE Journal of Photovoltaics* 7: 702–708.

12 Song, K., Han, J.H., Lim, T. et al. (2016). *Advanced Healthcare Materials* 5: 1572–1580.

13 Shockley, W. and Queisser, H.J. (1961). *Journal of Applied Physics* 32: 510–519.

14 Polman, A., Knight, M., Garnett, E.C. et al. (2016). *Science* 352: 4424.

15 Steiner, M.A., Geisz, J.F., Garcia, I. et al. (2013). *Journal of Applied Physics* 113: 123109.

16 Mattos, L.S., Scully, S.R., Syfu, M. et al. (2012). New module efficiency record: 23.5% under 1-sun illumination using thin-film single-junction GaAs solar cells. In: *2012 38th IEEE Photovoltaic Specialists Conference*, 3187–3190.

17 Yablonovitch, E., Gmitter, T., Harbison, J.P., and Bhat, R. (1987). *Applied Physics Letters* 51: 2222–2224.

18 Ando, K. and Yamaguchi, M. (1985). *Applied Physics Letters* 47: 846–848.

19 Coutts, T.J. and Naseem, S. (1985). *Applied Physics Letters* 46: 164–166.

20 Keavney, C., Haven, V., and Vernon, S. (1990). Emitter structures in MOCVD InP solar cells. In: *IEEE Conference on Photovoltaic Specialists*, 141–144.

21 Wanlass, M. (2017). Systems and methods for advanced ultra-high-performance InP solar cells. Google Patents.

22 Yin, X., Battaglia, C., Lin, Y. et al. (2014). *ACS Photonics* 1: 1245–1250.

23 Schubert, M., Gottschalch, V., Herzinger, C.M. et al. (1995). *Journal of Applied Physics* 77: 3416–3419.

24 Karam, N.H., King, R.R., Haddad, M. et al. (2001). *Solar Energy Materials & Solar Cells* 66: 453–466.

25 King, R.R., Fetzer, C.M., Colter, P.C. et al. (2002). High-efficiency space and terrestrial multijunction solar cells through bandgap control in cell structures. In: *Conference Record of the Twenty-Ninth IEEE Photovoltaic Specialists Conference*, 776–781.

26 Pla, J., Barrera, M., and Rubinelli, F. (2007). *Semiconductor Science and Technology* 22: 1122–1130.

27 Geisz, J.F., Steiner, M.A., Garcia, I. et al. (2013). *Applied Physics Letters* 103: 041118.

28 Yang, W.Q., Becker, J., Liu, S. et al. (2014). *Journal of Applied Physics* 115: 203105.

29 Takamoto, T., Ikeda, E., Kurita, H., and Ohmori, M. (1997). *Applied Physics Letters* 70: 381–383.

30 Sugiura, H., Amano, C., Yamamoto, A., and Yamaguchi, M. (1988). *Japanese Journal of Applied Physics* 27: 269–272.

31 Olson, J.M., Kurtz, S.R., Kibbler, A.E., and Faine, P. (1990). *Applied Physics Letters* 56: 623–625.

32 Takamoto, T., Ikeda, E., Kurita, H. et al. (1997). *Japanese Journal of Applied Physics* 36: 6215–6220.

33 NREL (2013). NREL Reports 31.1% Efficiency for III-V Solar Cell. https://www.nrel.gov/news/press/2013/2226.html (accessed 12 January 2019).

34 Jain, N., Schulte, K.L., Geisz, J.F. et al. (2017). GaInAsP/GaInAs tandem solar cell with 32.6% one-sun efficiency. In: *2017 IEEE 44th Photovoltaic Specialist Conference (PVSC)*.

35 Yamaguchi, M., Okuda, T., Taylor, S.J. et al. (1997). *Applied Physics Letters* 70: 1566–1568.

36 Baudrit, M. and Algora, C. (2010). *Physica Status Solidi A: Applications and Materials Science* 207: 474–478.

37 King, R., Law, D., Edmondson, K. et al. (2007). *Applied Physics Letters* 90: 183516.

38 King, R.R., Haddad, M., Isshiki, T. et al. (2000). Metamorphic GaInP/GaInAs/Ge solar cells. In: *Conference Record of the IEEE Photovoltaic Specialists Conference*, 982–985.

39 Sasaki, K., Agui, T., Nakaido, K. et al. (2013). *AIP Conference Proceedings* 1556: 22–25.

40 Wojtczuk, S., Chiu, P., Zhang, X.B. et al. (2010). InGaP/GaAs/InGaAs 41% concentrator cells using bi-facial epigrowth. In: *Proceedings of the 35th IEEE Photovoltaic Specialists Conference*, 1259–1264.

41 Dimroth, F., Guter, W., Schone, J. et al. (2009). Metamorphic GaInP/GaInAs/Ge triple-junction solar cells with > 41% efficiency. In:

34th IEEE Photovoltaic Specialists Conference. (PVSC), Philadelphia, PA, 1933–1937.

42 Sharp. (2013) http://www.sharp-world.com/corporate/news/130614.html.

43 Derkacs, D., Jones-Albertus, R., Suarez, F., and Fidaner, O. (2012). *Journal of Photonics for Energy* 2: 8.

44 Wiemer, M., Sabnis, V., and Yuen, H. (2011). 43.5% efficient lattice matched solar cells. In: *SPIE Solar Energy + Technology*, vol. 8108, 5. SPIE.

45 Bruel, M., Aspar, B., and AubertonHerve, A.J. (1997). *Japanese Journal of Applied Physics Part 1* 36: 1636–1641.

46 Cho, E.C., Green, M.A., Xia, J. et al. (2004). *Applied Physics Letters* 84: 2286–2288.

47 Bedell, S.W., Shahrjerdi, D., Hekmatshoar, B. et al. (2012). *IEEE Journal of Photovoltaics* 2: 141–147.

48 Bedell, S.W., Fogel, K., Lauro, P. et al. (2013). *Journal of Physics D: Applied Physics* 46.

49 Yoon, J., Jo, S., Chun, I.S. et al. (2010). *Nature* 465: 329–U380.

50 Thouless, M.D., Evans, A.G., Ashby, M.F., and Hutchinson, J.W. (1987). *Acta Metallurgica et Materialia* 35: 1333–1341.

51 Suo, Z. and Hutchinson, J.W. (1989). *International Journal of Solids and Structures* 25: 1337–1353.

52 Shahrjerdi, D. and Bedell, S.W. (2013). *Nano Letters* 13: 315–320.

53 Kim, Y., Cruz, S.S., Lee, K. et al. (2017). *Nature* 544: 340–343.

54 Konagai, M., Sugimoto, M., and Takahashi, K. (1978). *Journal of Crystal Growth* 45: 277–280.

55 Essig, S., Allebé, C., Remo, T. et al. (2017). *Nature Energy* 6: 17144.

56 Ahrenkiel, R.K., Dunlavy, D.J., Keyes, B. et al. (1989). *Applied Physics Letters* 55: 1088–1090.

57 Geisz, J.F., Friedman, D.J., Ward, J.S. et al. (2008). *Applied Physics Letters* 93: 123505.

58 Moon, S., Kim, K., Kim, Y. et al. (2016). *Scientific Reports* 6: 30107.

59 van Niftrik, A.T.J., Schermer, J.J., Bauhuis, G.J. et al. (2008). *Journal of the Electrochemical Society* 155: D35–D39.

60 Lee, J.W., Pearton, S.J., Abernathy, C.R. et al. (1995). *Journal of the Electrochemical Society* 142: L100–L102.

61 Yoon, J., Baca, A.J., Park, S.I. et al. (2008). *Nature Materials* 7: 907–915.

62 Lee, J., Wu, J.A., Shi, M.X. et al. (2011). *Advanced Materials* 23: 986–991.

63 Lee, J., Wu, J., Ryu, J.H. et al. (2012). *Small* 8: 1851–1856.

64 Yamaguchi, M. and Luque, A. (1999). *IEEE T. Electron. Dev.* 46: 2139–2144.

65 Swanson, R.M. (2000). *Progress in Photovoltaics* 8: 93–111.

66 Yoon, J., Li, L.F., Semichaevsky, A.V. et al. (2011). *Nature Communications* 2.

67 Mousazadeh, H., Keyhani, A., Javadi, A. et al. (2009). *Renewable and Sustainable Energy Reviews* 13: 1800–1818.

68 Sheng, X., Shen, L., Kim, T. et al. (2013). *Advanced Energy Materials* 3: 991–996.

69 Sansregret, J., Drake, J., Thomas, W., and Lesiecki, M. (1983). *Applied Optics* 22: 573–577.

70 Sheng, X., Yun, M.H., Zhang, C. et al. (2015). *Advanced Energy Materials* 5.

71 Hyldahl, M.G., Bailey, S.T., and Wittmershaus, B.P. (2009). *Solar Energy* 83: 566–573.

72 Wu, J.J. and Kortshagen, U.R. (2015). *RSC Advances* 5: 103822–103828.

73 Currie, M.J., Mapel, J.K., Heidel, T.D. et al. (2008). *Science* 321: 226–228.

74 Barnham, K., Marques, J.L., Hassard, J., and O'Brien, P. (2000). *Applied Physics Letters* 76: 1197–1199.

75 Meinardi, F., Ehrenberg, S., Dhamo, L. et al. (2017). *Nature Photonics* 11: 177–185.

76 Bronstein, N.D., Yao, Y., Xu, L. et al. (2015). *ACS Photonics* 2: 1576–1583.

77 Kim, J., Hwang, J., Song, K. et al. (2016). *Applied Physics Letters* 108: 253101.

78 Il Park, S., Shin, G., Banks, A. et al. (2015). *Journal of Neural Engineering* 12.

79 Chiu, P., Law, D., Woo, R. et al. (2014). *IEEE Journal of Photovoltaics* 4: 493–497.

80 King, R.R., Fetzer, C.M., Law, D.C. et al. (2006). Advanced III–V multi-junction cells for space. In: *Conference Record of the 2006 IEEE 4th World Conference on Photovoltaic Energy Conversion, WCPEC-4*, 1757–1762.

81 Kim, B.J., Kim, D.H., Lee, Y.Y. et al. (2015). *Energy & Environmental Science* 8: 916–921.

82 Bereuter, L., Williner, S., Pianezzi, F. et al. (2017). *Annals of Biomedical Engineering* 45: 1172–1180.

83 Takamoto, T., Washio, H., and Juso, H. (2014). Application of InGaP/GaAs/InGaAs triple junction solar cells to space use and concentrator photovoltaic. In: *IEEE 40th Photovoltaic Specialist Conference (PVSC)*, 0001–0005.

84 Dimroth, F., Tibbits, T.N.D., Niemeyer, M. et al. (2016). *IEEE Journal of Photovoltaics* 6: 343–349.

85 Luque, A. (2011). *Journal of Applied Physics* 110: 031301.

86 Friedman, D.J. and Kurtz, S.R. (2002). *Progress in Photovoltaics* 10: 331–344.

87 Zhang, Y., Wang, Q., Zhang, X.B. et al. (2016). *Chinese Physics Letters* 33.

88 King, R.R., Boca, A., Hong, W. et al. (2009). Band-gap-engineered architectures for high-efficiency multijunction concentrator solar cells. In: *24th European Photovoltaic Solar Energy Conference and Exhibition, Hamburg, Germany*, vol. 21, 55.

89 France, R.M., Geisz, J.F., Garcia, I. et al. (2016). *IEEE Journal of Photovoltaics* 6: 578–583.

90 Zhao, L., Flamand, G., and Poortmans, J. (2010). *AIP Conference Proceedings* 1277: 284–289.

91 Sheng, X., Bower, C.A., Bonafede, S. et al. (2014). *Nature Materials* 13: 593–598.

92 Cotal, H., Fetzer, C., Boisvert, J. et al. (2009). *Energy & Environmental Science* 2: 174–192.

93 Hopkinson, M., Martin, T., and Smowton, P. (2013). *Semiconductor Science and Technology* 28: 090301.

94 Wang, Z.C., Van Gasse, K., Moskalenko, V. et al. (2017). *Light: Science & Applications* 6.

95 Mohseni, P.K., Behnam, A., Wood, J.D. et al. (2014). *Advanced Materials* 26: 3755–3760.

96 Xiong, K., Lu, S., Dong, J. et al. (2010). *Solar Energy* 84: 1975–1978.

97 Huang, Q.L., Wang, J.Z., Quan, B.G. et al. (2013). *Applied Optics* 52: 2312–2319.

98 Mojiri, A., Taylor, R., Thomsen, E., and Rosengarten, G. (2013). *Renewable and Sustainable Energy Reviews* 28: 654–663.

99 Goetzberger, A., Goldschmidt, J., Peters, M., and Löper, P. (2008). *Solar Energy Materials & Solar Cells* 92: 1570–1578.

100 Arbabi, E., Arbabi, A., Kamali, S.M. et al. (2017). *Optica* 4: 625–632.

101 Ganapati, V., Steiner, M.A., and Yablonovitch, E. (2016). *IEEE Journal of Photovoltaics* 6: 801–809.

102 Ganapati, V., Ho, C.S., and Yablonovitch, E. (2015). *IEEE Journal of Photovoltaics* 5: 410–417.

103 Garcia, I., Kearns-McCoy, C.F., Ward, J.S. et al. (2014). *Applied Physics Letters* 105.